

ARTICLE OPEN



Coherent memory for microwave photons based on long-lived mechanical excitations

Yulong Liu¹✉, Qichun Liu¹, Huanying Sun¹, Mo Chen¹, Shuaipeng Wang² and Tiefu Li³✉

Mechanical resonators, due to their capability to host ultralong-lived phonon modes, are particularly attractive for quantum state storage and as memory elements in conjunction with quantum computing and communication networks. Here we demonstrate absorptive-type coherent memory based on long-lived mechanical excitations. The itinerant coherent microwave field is captured, stored, and retrieved from a mechanical memory oscillator which is pre-cooled to the ground state. The phase space distribution allows us to distinguish between coherent and thermal components and study their evolution as a function of storage time. Our device exhibits attractive functions with an energy decay time of $T_1 = 15.9$ s, a thermal decoherence rate of $\Gamma_{\text{th}} = 2.85$ Hz, and acquires less than one quantum noise during the $\tau_{\text{coh}} = 55.7$ ms storage period. We demonstrate that both the amplitude and phase information of microwave coherent states can be recovered, indicating the coherence of our memory device. These results suggest that high-Q mechanical resonators and long coherence time phonons could be ideal candidates for the construction of long-lived and on-demand microwave quantum memories.

npj Quantum Information (2023)9:80; <https://doi.org/10.1038/s41534-023-00749-x>

INTRODUCTION

Quantum memories are core quantum building blocks and are at the very heart of, e.g., storing fault-tolerant surface codes for quantum computing^{1–3} and building quantum repeaters for long-distance quantum communication^{4–6}. Emissive quantum memories of the built-in type have been used to realize heralded two-excitation entanglement, e.g., based on the atom-photon interactions^{7–11}. Absorptive quantum memories, e.g., those based on rare-earth-ion-doped crystals, can overcome the trade-off between multiplexing capacity and deterministic properties^{12–21}. Optomechanical memory can be absorptive-type and combine the most important characteristics of high efficiency, long storage time, and multiqubit capacity^{22–26}. Moreover, they can store quantum states encoded in microwaves as well as in optical photons^{27–30}. Thus, optomechanical memory shows great potential in combining quantum computing and communication devices to build universal quantum networks^{31–33}. Classical optical information storage as mechanical oscillation has been demonstrated in, e.g., a silica optomechanical resonator^{34–36} and diamond microdisk³⁷, showing a storage time of approximately a few microseconds. Optical quantum memory at telecom wavelengths was realized based on silicon optomechanical crystals wherein a mechanical resonance at a few gigahertz was thermalized to milli-Kelvin temperature^{38,39}.

In the microwave domain, the implementations of optomechanical interaction typically behave as a microwave cavity capacitively coupled to a moving mechanical resonator with kilohertz or megahertz vibration frequency⁴⁰. Using parametrical coupling to swap states between microwave and mechanical memory has the advantages of, e.g., not requiring frequency resonance matching^{41–49}, achieving near-unit efficiency^{50–55}, and low-noise operation of a superconducting qubit^{56,57}. Superconducting drum mechanical resonators made of aluminum have been used to show microwave coherent state storage that adds less than one

quantum of noise⁵⁸. Subsequently, propagating microwave qubits encoded as superpositions of zero and one photons are successfully stored inside an aluminum micromechanical resonator with a fidelity in excess of the classical bound⁵⁹. For the above microwave optomechanical memories, the state storage lifetime is given by tens of microseconds, which mainly depends on the decoherence rate of the mechanical memory modes.

Meanwhile, silicon nitride (SiN) membrane resonators have been optomechanically coupled to optical^{60–70} or microwave cavities^{71–81}. Rational exploitation of the spatial distribution of mechanical modes enables simultaneous coupling of the SiN membrane resonator to both superconducting microwave and optical cavity resonators^{82,83}. Based on microwave field back-action, millimeter-sized SiN membrane resonators have reached their ground-state^{75–77}. Silicon-nitride (SiN) membranes with high stress have a mechanical mode quality factor (Q) in excess of 10^7 , measured in the cryostat^{71–75}. On the other hand, by incorporating phononic bandgap engineering with a SiN membrane⁷⁷, the Q -value of the mechanical modes can be further improved in excess of 10^9 . The coherent time in principle can arrive at a hundred milliseconds. Thus, it is very intriguing to build a microwave coherent memory device based on high- Q SiN mechanical membranes.

In this work, we develop an on-chip and absorptive-type superconducting cavity electromechanical device with a high-stressed SiN membrane mechanical resonator. We then systematically study the microwave state capture, storage, and retrieval dynamics with writing and reading operations. By matching the signal pulse amplitude growth rate to the sideband writing rate, the prepared field could be fully captured and stored as coherent mechanical excitations. The state tomography of the itinerated microwave pulse and mechanical memory resonator in their quadrature phase-space further allows for distinguishing between coherent and thermal components and studying their evolution as

¹Beijing Academy of Quantum Information Sciences, Beijing 100193, China. ²Quantum Physics and Quantum Information Division, Beijing Computational Science Research Center, Beijing 100193, China. ³School of Integrated Circuits and Frontier Science Center for Quantum Information, Tsinghua University, Beijing 100084, China.

✉email: liuyul@baqis.ac.cn; litf@tsinghua.edu.cn

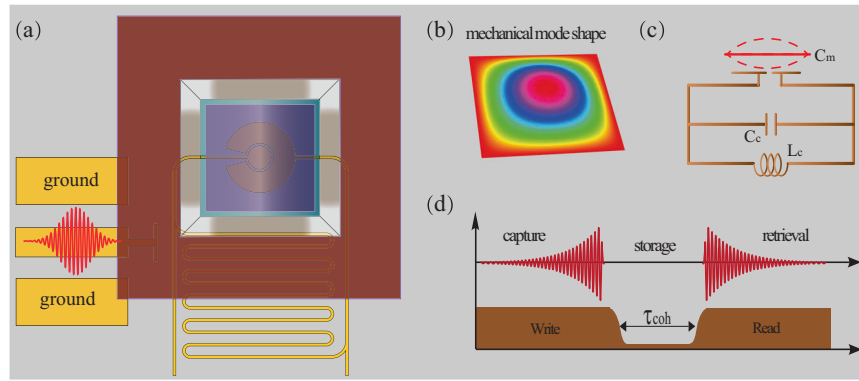


Fig. 1 On-chip superconducting electromechanical memory and state tomography pulse sequence. **a** The cavity electromechanical devices are mainly composed of a niobium microwave cavity and SiN film mechanical resonator. The pac-man-shaped microwave circuits are rendered in yellow, and the microwave signals couple in and out of the cavity through a common coplanar waveguide (CPW). The silicon-nitride chip consists of a $525\ \mu\text{m}$ thick silicon frame (rendered in red) with a central $500\ \mu\text{m}$ wide square film window (rendered in light blue). The suspended SiN-membrane is $50\ \text{nm}$ thick. A $20\ \text{nm}$ -thick aluminum film (rendered in purple) is deposited from the backside window of the chip, which covers all the SiN membrane. **b** The finite-element simulation (FEM) shows the vibration fundamental modes of the SiN membrane. **c** Schematic showing the placement of the metalized membrane over the antenna pads. The lumped-element model consists of the cavity capacitance C_c , inductance L_c , and mechanical capacitance C_m . **d** The upper trace depicts the probe signal, which has an exponential rising envelope. The probe signal has been captured, stored, and finally retrieved (shown as an exponentially decaying pulse). The bottom trace illustrates the corresponding write and read fields for the capture and retrieval processes, respectively.

a function of the storage time. Our system can store microwave coherent states with different amplitudes and phases, indicating coherence properties in the memory processes. The storage lifetime and decoherence rate are important figures of merit for characterizing a coherent memory. Our experiment shows that mechanical memory based on the SiN membrane resonator can yield a storage lifetime of tens of milliseconds, which is three orders of magnitude beyond the typical performance of other state-of-art microwave electromechanical devices.

RESULTS

The cavity electromechanical memory device

As shown in Fig. 1a, the cavity electromechanical device consists of a rattlesnake-like superconducting niobium (Nb) cavity and a mechanically compliant capacitor made of SiN membranes. We use a commercial ACC μ RA flip-chip bonder to align the center of the square SiN membrane window with the center of the bottom coupling electrode (concentric ring structure) of the microwave cavity. After the flip-chip package, a thin film of superconducting aluminum (Al) is deposited on top of the SiN membrane through an inverted tapered window on the back of the SiN-chip. Finally, the metallized SiN film will form a mechanical parallel-plate capacitor with the bottom rattlesnake microwave coupler. Compared with the traditional process of first metallizing the front side of the silicon nitride film and then flip-chip packaging^{71–78}, the dielectric of the mechanical capacitor in this work additionally contains silicon nitride, and the cleanliness of the front side of the film is better guaranteed. Therefore, the vacuum gap (mechanical capacitance) can be as small (large) as possible, to improve the microwave cavity electromechanical coupling strength. We here build a coherent mechanical memory based on the fundamental vibration mode of the SiN membrane.

The finite-element-simulation (FEM) of its vibration shape is shown in Fig. 1b, and the center of the membrane will move up and down. The gap between the metal Al film on the SiN membrane and the bottom coupling electrode of the cavity resonator is expected to be defined by the nanosized particles. However, the real case is more complex, for example, the final capacitor gap also depends on the deformation during the cool down in the dilution refrigerator. Detailed fabrication processes are given in the Supplementary Note 1.

The floating mechanical capacitor is connected in parallel to the microwave cavity resonator, loading the fundamental cavity resonance frequency down to $\omega_c/2\pi = 5.78\ \text{GHz}$. The efficient lumped-element model is shown in Fig. 1c. The membrane up and down vibrations change the mechanical capacitance, which in turn modifies the microwave cavity resonant frequency. The displacement of the silicon nitride film depends on the cavity-field radiation pressure (proportional to the number of photons in the cavity), forming dispersive optomechanical coupling. The CPW connector provides an external coupling ($\kappa_e/2\pi = 125.6\ \text{kHz}$) for performing input and output measurements. A coherent pump tone with frequency Ω_p and amplitude ξ is used to enhance the optomechanical coupling⁴⁰. In this experiment, the pump frequency is red-detuned to the cavity resonance (ω_c) by a mechanical frequency of $\omega_m/2\pi = 720.531\ \text{kHz}$, viz., $\Omega_p = \omega_c - \omega_m$. The total cavity decay rate ($\kappa/2\pi = 208.2\ \text{kHz}$) is smaller than the mechanical frequency. Thus, the system works in the resolved sideband regime, viz., $\omega_m > \kappa$. This results in an interaction reminiscent of a beam splitter, $H_{BS}/\hbar = G(a^\dagger b + b^\dagger a)$, where G represents the excitation exchange rate between photons and phonons and a and b are the annihilation operators for the microwave cavity and mechanical modes, respectively.

For this system, the writing and readout pump tones can control the effective coupling rate between cavity field and the mechanical displacement. As shown in Fig. 1d, for the storage process, a writing pump tone couples a signal pulse into the mechanical mode, generating mechanical excitations. For the retrieval process, a readout pulse couples the stored mechanical excitation to the cavity mode, mapping the mechanical excitation back to a microwave pulse. Note that the optomechanical storage and retrieval processes can, in principle, preserve the phase coherence of the injected state.

Sideband cooling of the fundamental mechanical mode

A major impediment to achieving coherent storage using mechanical excitations is the noise added by thermal occupation of this mechanical mode. For optomechanical memory, both the thermal noise of the cavity and mechanical modes are involved in the state capture, storage, and retrieval processes and thus contribute to the added noise of the stored target state. To minimize such superimposed thermal noise, an ideal optomechanical memory should operate with both the cavity and mechanical

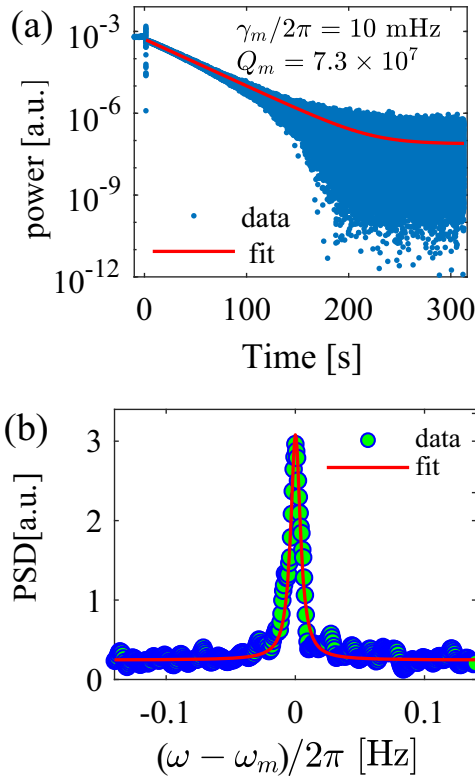


Fig. 2 Mechanical ringdown and spectrum measurements. **a** A mechanical energy ring-down measured at 10 mK, showing a decay rate of $\gamma_m/2\pi = 10$ mHz. **b** The PSD of the mechanics obtained from the IQ measurement with a 1000 s sampling time. The spectrum linewidth via Lorentz fit is $\gamma_m/2\pi = 10.2$ mHz.

modes in its ground-state. We then show effective optomechanical sideband cooling to prepare mechanical oscillators toward their ground state.

The device is placed on a mechanical eddy-current damper (hanging on the mixing chamber cold plate of a Bluefors dilution refrigerator) to isolate external mechanical vibration noises, including pulsed tube vibrations⁷⁸. As shown in Fig. 2a, an energy ring-down measurement clearly exhibits that the fundamental drumhead mode of the mechanical membrane has a frequency of $\omega_m/2\pi = 720.531$ kHz, and a decay rate of $\gamma_m/2\pi = 10$ mHz, corresponding to $Q_m = 7.2 \times 10^7$. The stoichiometric SiN-membrane windows have a high tensile stress (~ 0.9 GPa), which could divert material losses and mitigate edge anchor losses.

We drive the electromechanical system with a microwave tone at a fixed angular frequency Ω_p , which is red-detuned from the cavity resonance by the mechanical frequency $\Delta = \Omega_p - \omega_c = -\omega_m$. Under a low power (e.g., -33 dBm at the source output port), the microwave field dynamic backaction is negligible, and we can obtain the mechanical Lorentzian spectrum [Fig. 2b] based on the power spectrum density (PSD) measurements. The measurement setups are described in the Supplementary Note 2.

We now calibrate the initial phonon occupation of the fundamental mechanical mode of the SiN membrane resonator. In Fig. 3a, we show the average phonon occupation as a function of the refrigerator's temperature. We assumed that the phonon occupation of the mechanical resonator can arrive at its equilibration at several hundred millikelvin (mK) temperatures provided by the cryostat. Using Bose-Einstein statistics for thermal states $N_m^{\text{th}} = (e^{\hbar\omega_m/k_B T_{\text{bath}}} - 1)^{-1}$, we extract a calibration constant between the mechanical sideband area and mechanical occupation in quanta. We expect the mechanical spectrum area to

increase accordingly if the mechanical mode environment is at the refrigerator's temperature. Indeed, above the refrigerator's (Bluefors LD400) base temperature of 10 mK, we found that the spectrum area is proportional to the refrigerator's temperature, as shown in Fig. 2a. From the above analysis, we infer that the mechanical mode can be thermalized to a bath at $T_{\text{bath}} = 10$ mK, corresponding to an initial phonon occupation of $N_m^{\text{th}} = 285.6$.

We carried out sideband cooling of the fundamental mechanical mode of the SiN membrane. To reduce the steady-state phonon occupation, we drive the microwave cavity precisely on its red-sideband with a fixed detuning given by the mechanical frequency, viz., $\Omega_p = \omega_c - \omega_m$. Under such frequency mismatch conditions, the mechanical frequency shift due to the dynamical backaction is close to zero, but the effective damping rate depends on the power of microwave radiation pressure (resulting in dynamical backaction cooling). A variable attenuator and phase shifter are combined to cancel the reflected drive power before the HEMT amplification. The other measurement conditions are the same as those used to calibrate the initial thermal phonon occupation.

Under current pump parameters, the effective optomechanical coupling rate G between the microwave cavity and the mechanical mode is proportional to $\sqrt{n_d}$, viz., $G = g_0 \sqrt{n_d}$. Here, g_0 is the single-photon optomechanical coupling strength, and n_d is the average number of photons in the microwave cavity, which is linear in the sideband pump power $n_d \propto P$. We found that the passivated niobium superconducting resonator can improve the stability of the cavity linewidth. Figure 3b demonstrates that the microwave cavity has relatively stable internal and external dissipation rates with increasing sideband pump driving strength. As also shown in Fig. 3b, the parametric coupling strength G increased linearly with \sqrt{P} . The cavity radiation-pressure coupling broadens the linewidth of the mechanical mode with an additional damping rate of $\gamma_{\text{opt}} = 4G^2/k$, which is linear to sideband pump power P . Therefore, in the logarithmic coordinates used in Fig. 3b, the slope of γ_{opt} is twice the slope of G as a function of driving power P . The mechanical mode ring-down spectra under different radiation-pressure damping γ_{opt} are presented in the Supplementary Note 3.

In our experiment, the maximum linewidth of the damped mechanical mode does not exceed one percent of the microwave cavity linewidth ($|\omega - \omega_c| \ll \kappa$), and the device works inside the resolved-sideband regime ($\omega_m \gg \kappa$). Under such conditions and resorting to the quantum mechanical description of the microwave electromechanical circuit, the expected power spectral density in units of noise quanta is given by:

$$\frac{S[\omega]}{\hbar\omega} = \frac{1}{2} + n_{\text{add}} + 2\kappa_e \frac{\kappa \bar{N}_c^{\text{th}} (\gamma_m^2 + 4\delta^2) + 4\gamma_m N_m^{\text{th}} G^2}{|4G^2 + (\kappa + 2i\delta)(\gamma_m + 2i\delta)|^2}, \quad (1)$$

where $i = \sqrt{-1}$, $\delta = \omega - \omega_m$, and n_{add} is the added noise of the microwave measurement, which mainly comes from the HEMT amplifiers. The added noise expressed as the equivalent microwave photon number contributes to the background noise floor of the measured PSD spectra. Here, we have defined $\bar{N}_c^{\text{th}} = \eta N_c^{\text{th}}$, with $\eta = \kappa_e/\kappa$. N_c^{th} represents the effective thermal noise occupation of the cavity mode. The cavity thermal noise spectrum is a Lorentzian type, and its linewidth depends on the cavity decay rate κ . N_m^{th} is the effective thermal occupation of the mechanical mode, which is featured as a Lorentzian spectrum with a linewidth of $\gamma_{\text{eff}} = \gamma_m + \gamma_{\text{opt}}$, and γ_{opt} is the "optical" damping introduced by the dynamical backaction of the microwave cavity field.

Figure 3 (c) shows the mechanical PSD (blue curves) and Lorentz fits (red curves) for five different driver powers. As expected, the fundamental mechanical mode of the SiN membrane can be cooled as the driving power P is increased from -25 dBm to 15 dBm. With lower driving power [e.g., $P = -30$ dBm in Fig. 3b], the optical damping is negligible

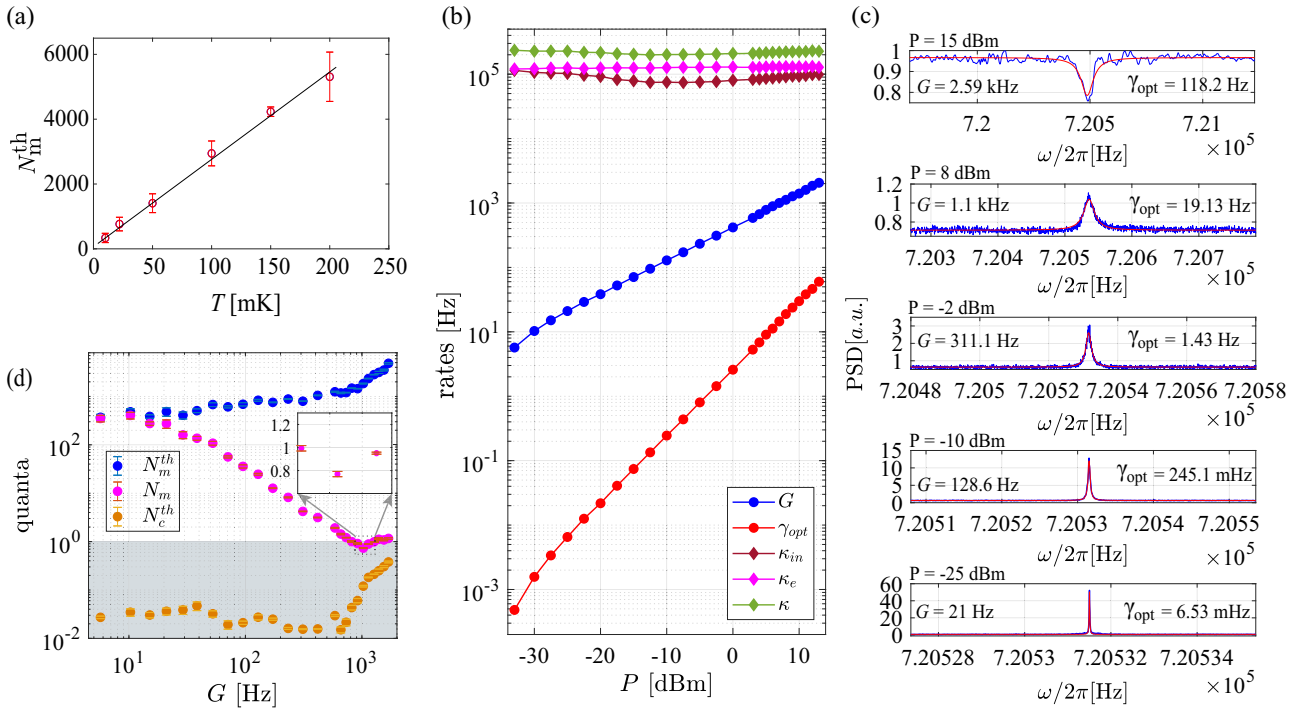


Fig. 3 Sideband cooling of the mechanical memory mode. **a** The thermal occupancy of the mechanical mode calibrated by sweeping the cryostat temperature. The mechanical mode starts its thermal equilibrium with the cryostat at $T = 10$ mK, corresponding to an initial thermal phonon occupation of $N_m^{\text{th}} = 285.6$. Error bars represent the standard deviation. **b** The measured cavity decay rates (κ_{in} , κ_e , κ), parametric coupling rates G , and optical damping rates γ_{opt} at each sideband pump power. **c** The PSD (blue curves) and Lorentzian fits (red curves) for five different sideband pump powers. From bottom to top with a higher pump power, the mechanical mode linewidth becomes broader, and the mode is cooled by the microwave photon radiation pressure. **d** Sideband cooling reduces the thermal occupation of the mechanical mode (calibrated in number of motional quanta) below one phonon, reaching a minimum of $N_m = 0.78$. The thermal occupations of the microwave cavity (N_c^{th}) and mechanical resonator (N_m^{th}) baths increase under higher sideband pump power. Error bars are standard deviations.

($\gamma_{\text{opt}} = 1.57$ mHz $\ll \gamma_m$); therefore, the PSD spectrum has a standard Lorentzian shape whose area is proportional to an initial thermal occupation of $N_m^{\text{th}} = 285.6$. This defines the regime (with driving power below -30 dBm) where we calibrate the mechanical mode linewidth and its initial thermalization temperature from the cryostat. With higher driving power, the mechanical PSD is damped with a broadened linewidth and cooled down with a smaller spectrum area, as shown in Fig. 3c. Based on optical damping, the phonon damping rate exceeds the extraction rate from the mechanical thermal bath, leading to cooling of the mechanical mode. Finally, in the steady-state, a new equilibrium is established with reduced average phonon occupation ($N_m < N_m^{\text{th}}$), corresponding to a lower temperature for this mechanical mode.

Under strong driving, the noise floor starts to rise, and EIT-like Lorentz dips are observed in Fig. 3(c). At the maximum driving power ($P = 15$ dBm) used in this work, spectrum squashing appears as a result of interference between the mechanical and cavity noises. Here, the microwave noise (corresponding to N_c^{th}) plays a significant role and the cavity heating may come from either the pump tone phase noise or direct heating of the cavity circuit. In fact, the thermal occupations for both N_c^{th} and N_m^{th} are variable and related to the sideband pump power.

Using the function given in Eq. (1) and through the nonlinear least-squares fitting of the PSD gives the instant number of N_c^{th} and N_m^{th} under different sideband pump powers. We can then calculate the final mechanical occupation as:

$$N_m = N_m^{\text{th}} \left(\frac{\gamma_m}{\kappa} \frac{4G^2 + \kappa^2}{4G^2 + \kappa\gamma_m} \right) + N_c^{\text{th}} \left(\frac{4G^2}{4G^2 + \kappa\gamma_m} \right). \quad (2)$$

Equation (2) indicates that sideband cooling can never reduce the mechanical mode occupancy below the cavity occupancy. Therefore, N_c^{th} must remain smaller than one quantum to achieve

ground state cooling. The cavity thermal bath (N_c^{th}), mechanic thermal bath (N_m^{th}) and mechanical mode steady-state occupations are summarized in Fig. 3(d), as a function of coupling rate G . When the driving power reaches $P = 8$ dBm, the average phonon occupation N_m is reduced below one quantum of mechanical motion, reaching the quantum regime. In this experiment, the minimum average phonon occupation is $N_m = 0.78$, which is limited by the mechanical and cavity mode heating (bath temperature rises).

Coherent-state capture, storage and retrieval

We then investigate its performance as a memory by measuring the capture, storage, and retrieval of itinerant microwave pulses in the time domain. From the beam-splitter-like optomechanical interaction $H_{\text{BS}} = G(a^\dagger b + b^\dagger a)$, it is obvious that by controlling the pulse sequence of the transfer field, we can write the itinerant microwave pulse into and out of the mechanical resonator.

As depicted in Fig. 4(a), we add a constant sideband cooling tone (300 ms from t_0 to t_1) to initialize the mechanical memory to its ground state, $N_m = 0.78$ with $\gamma_{\text{opt}} = 19.13$ Hz. Subsequently, we write a microwave pulse with energy that grows exponentially at a given rate of $\Gamma = \gamma_{\text{opt}}$, and it is sent inside the cavity resonator from that moment of t_1 . From t_1 to t_2 (duration 60 ms), the constant sideband cooling tone is still on and plays another role, transferring the microwave pulse into the SiN membrane resonator. Meanwhile, the microwave coherent state is captured, and the coherent portion of the mechanical mode continuously increases. In this stage, the sideband cooling tone writes the pulse signal into mechanical excitations, and thus, it is also called the write field.

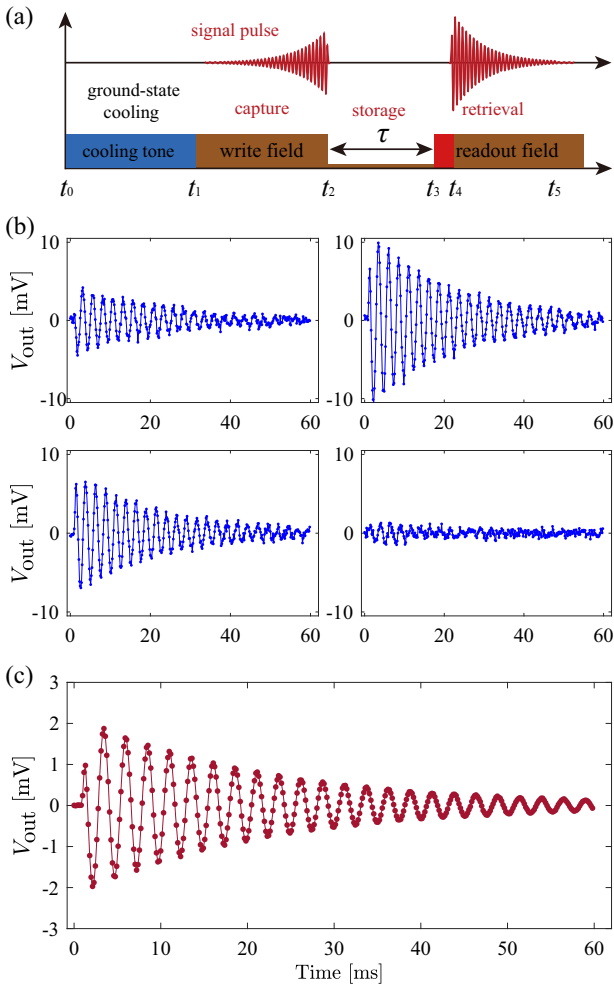


Fig. 4 Coherent-state capture, storage and retrieval. **a** The diagram depicts the protocol for optomechanical capture, storage and retrieval of an itinerant microwave pulse within one transfer-field pulse sequence. **b** The voltage V_{out} generated in the CPW transmission line by the circuit is amplified and then digitized by the spectrum analyser. The voltage signal is mixed down to $\omega_s = 400$ Hz. The measured V_{out} from four independent measurements using the pulse sequence depicted in (a), and (c) plots the coherent portion of V_{out} by averaging 2000 repetitions of the sequences.

At the moment of t_2 , the constant cooling tone (i.e., the write field) is closed, and the microwave coherent state has been stored inside the mechanical memory. Using an optomechanical phase-insensitive amplification technique with a blue-detuned sideband pump^{84,85}, we achieve $G^{\text{blue}} \simeq 46.8$ dB gain for the mechanical motional sideband. The amplification process continues 30 ms from t_3 to t_4 with an optomechanical anti-damping rate of $\Gamma_{\text{amp}}/2\pi = 53.5$ Hz. After a certain period of storage (τ), the constant sideband cooling tone is added again (60 ms from t_4 to t_5), which maps the state of the mechanical resonator back to the itinerant microwave pulse. In this stage, the constant sideband cooling tone allows us to retrieve the microwave coherent state, and thus, we also call it the readout field. From t_0 to t_5 , we complete a whole pulse consequence [as depicted in Fig. 4a] including the capture, storage, and retrieval of an itinerant microwave pulse.

It is notable that during the state storage procedure (with a time of τ), the mechanical mode undergoes an energy decay at a rate of $\gamma_m/2\pi = 10$ mHz (corresponding to $T_1 = 15.915$ s) and thermal decoherence ($\Gamma_{\text{th}}/2\pi = 2.85$ Hz). Thus, the retrieved microwave pulse must contain some thermal noise with amplitudes that should follow the Gaussian distribution. Taking the example of

storing two seconds ($\tau = 2$ s), the digitized voltage signal is mixed down to $\omega_{\text{out}} = 400$ Hz, and Fig. 4b show the voltage wave (V_{out}) of four independent measurements. Comparing each test, the amplitude of V_{out} presents a certain randomness. However, the statistical results after repeated measurements should show a Gaussian distribution. We then obtain the coherent portion, as shown in Fig. 4c, from the digitized voltage by averaging 2000 repetitions of the protocol. The decay rate of V_{out} is determined by $\gamma_{\text{opt}}/2$. Here, the exponential fit result is $\gamma_{\text{opt}}/2\pi = 19.56$ Hz, which keeps in correspondence with measured optical damping presented in the sideband cooling section.

We now directly present the coherent storage lifetime by recording its thermal decoherence in the time domain. Turning on the readout field, the amplitude and phase of V_{out} encode the state of the mechanical mode after a storage time of τ . The readout field retrieves the microwave pulse whereby the state of the mechanical mode is mapped. Therefore, realizing state tomography of the retrieved microwave field also means realizing state tomography of the mechanical oscillator at the moment the readout field is turned on.

As presented in Fig. 4b, we know the oscillation frequency (ω_{out}) and energy exponential decay rate (γ_{opt}) of the measured voltage signal V_{out} . This allows us to extract the amplitude and phase information of the microwave temporal mode from each independent pulse sequence measurement. Meanwhile, we can infer the state of the mechanical oscillator at the moment of turning on the readout field. The uncalibrated quadratures of motion are obtained by projecting V_{out} onto the oscillator with frequency ω_{out} :

$$\begin{aligned} X_1 &= S \sum_i V_{\text{out}}(t_i) \cos(\omega_{\text{out}} t_i), \\ X_2 &= S \sum_i V_{\text{out}}(t_i) \sin(\omega_{\text{out}} t_i). \end{aligned} \quad (3)$$

The completion of each transfer-field pulse sequence will allow us to obtain an output voltage (V_{out}) of the retrieved microwave pulse and produce a single point in the quadrature phase space. Repeating the transfer-pulse sequence allows us to obtain the quadrature distribution of the retrieved microwave pulse. Based on the state tomography, we can distinguish the portion of coherent mechanical excitations $N_{\text{coh}} = \langle X_1^2 \rangle + \langle X_2^2 \rangle$ and the thermal component $N_{\text{th}}^r = \langle (X_1 - \langle X_1 \rangle)^2 \rangle + \langle (X_2 - \langle X_2 \rangle)^2 \rangle - N_{\text{add}}$. Brackets here represent an ensemble average.

We calibrate the thermal (N_{th}^r) and coherent (N_{coh}) phonon numbers in units of quanta by sweeping the operating temperature (T_{cry}) of the cryostat from 10 mK to 140 mK. We waited a relatively long time (≥ 1 h) to ensure that the mechanical mode reached thermal equilibrium, and then we conducted the state tomography by repeating the pulse sequences 1000 times for each working temperature. We know that the variance of $X_{1,2}$ depends on the mode temperature (T_{bath}) as $N_m^{\text{th}} = \langle X_1^2 \rangle + \langle X_2^2 \rangle + N_{\text{add}}$. From the temperature sweep experiment (see Supplementary Note 4), we found that the variances increase linearly with temperature. The sweeping-temperature experiment based on pulsed measurements confirms again that the mechanical mode can be thermalized to the fridge operating temperature (including base temperature), viz, $T_{\text{bath}} = T_{\text{cry}}$. Recalling the Bose-Einstein statistics for thermal states $N_m^{\text{th}} = (e^{\hbar\omega_m/k_B T_{\text{bath}}} - 1)^{-1}$, we can calibrate the gain-factor S in Eqs. (3) and express $X_{1,2}$ in units of quanta.

The scatter plots of the measured quadratures are presented in Fig. 5(a) where the points are 3000 independent measurements with the cryostat operating at its base temperature, $T_{\text{base}} = 10$ mK. Figure 5a show the measured quadratures for different storage intervals, $\tau = 0$ s, 0.5 s, 5 s, 80 s, respectively. The red-histograms with normal distribution fit (black-curves) verify the Gaussian distribution of the thermal noise (with an average thermal phonon number N_{th}^r). The offset of the center of the scatter plot relative to

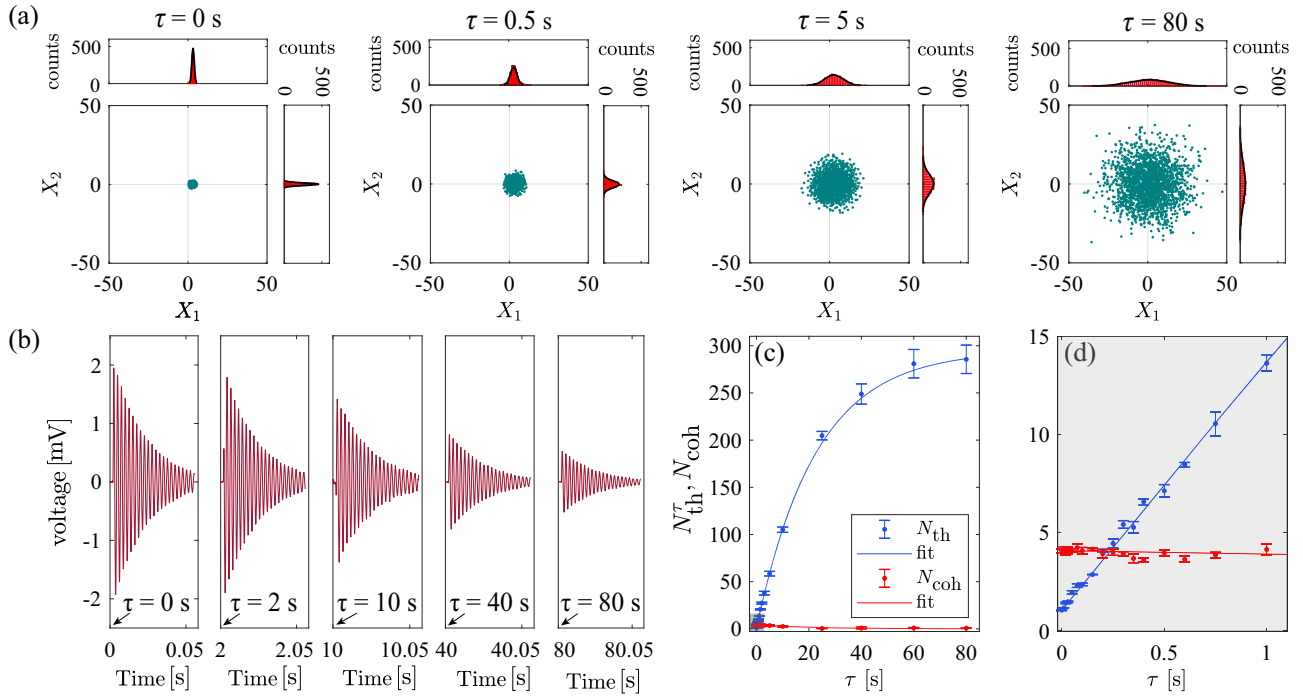


Fig. 5 State tomography and revolution versus time. **a** State tomography of transmitted microwave pulse. The scatter plot shows the measured quadrature amplitudes for different storage times $\tau = 0, 0.5, 5, 80$ s. A pulse sequence measurement yields a single point in such quadrature phase space, and each figure in **(a)** contains 2784 independent sequence measurements. The offset of the center of the quadrature distribution relative to the origin of the coordinates corresponds to the coherent component of the retrieval signal, and the red-histograms verify the Gaussian distribution of the added thermal noise. **b** The coherent component of the retrieved transmit signal after a storage time of, e.g., $\tau = (0, 2, 10, 40, 80)$ s. **c** The coherent and thermal components of the retrieved transmit signal are measured as a function of storage time τ . **d** Magnified view of the grey shaded area in **(c)**. The blue (red) dots (with error bars) in **(c)** and **(d)** are experimental data of thermal (coherent) occupation N_{th}^T (N_{coh}), while the solid lines are the corresponding exponential fit. Error bars represent the standard deviation.

the origin of the coordinates represents the component of the coherent excitations N_{coh} . As the storage interval τ increases, the variance $\sigma^2 = N_{th}^T$ starts to increase due to thermal decoherence. At the same time, the center of the scatter points moves toward the origin of the coordinates, and the mean value of $X_{1,2}$ gradually approaches zero, indicating an energy decay of coherent phonons. By averaging the output voltage corresponding to each point in the scatter plots, we obtain the coherent portion of V_{out} after a specific storage interval τ . A series of measured coherent phonon signals for different τ are shown in Fig. 5b, and we find that the amplitude decreases with increasing storage time τ .

When the storage interval is zero, i.e., $\tau = 0$, we write in the pulse signal and create coherent mechanical excitations. The scatter plots [as shown in Fig. 5a] correspond to the state tomography of the initialized mechanical oscillator in its ground state. The coherent mechanical excitation as the coherent portion of V_{out} is shown in Fig. 5b, correspondingly. Within a period of storage τ , the mechanical memory is gradually thermalized, and the coherent phonon component also undergoes a decay. As shown in the last panel of Fig. 5b, the amplitude of V_{out} , corresponding to coherent phonon N_{coh} , decays to one-eighth of the original amplitude after the $\tau = 80$ s storage interval. Meanwhile, the variance of $X_{1,2}$ (corresponding to N_{th}^T) reaches the maximum value and stabilizes, indicating that the mechanical mode arrives at thermal equilibrium with the surrounding environment reservoir. The itinerant microwave pulse used in Fig. 5 results in coherent mechanical excitation of $N_{coh} = 4$. We have confirmed that such a weak itinerant microwave pulse will not introduce additional technical heating. Increasing the microwave pulse strength until $N_{coh} > 30$, the mechanical mode starts to heat up.

The coherent and thermal occupancies of the mechanical memory are measured as a function of the storage time interval τ , as shown in Fig. 5c. The mechanical memory takes 80 s for the free evolution from its ground state to a fully thermal equilibrium state. The fit of N_{coh} results in $\gamma_m/2\pi = 10 \pm 0.42$ mHz, which agrees well with the value measured from the ringdown and PSD measurements [Fig. 2a, b]. The storage lifetime is an important figure of merit for characterizing a coherent memory. The gray-shade area of Fig. 5c shows the thermalization and energy decay of the mechanical memory in shorter evolution intervals. Figure 5d shows the zoom-in plot of such a gray-shaded region. The storage lifetime is determined by the thermal decoherence rate of the mechanical memory, which is calibrated as $\Gamma_{th}/2\pi = 2.85 \pm 0.12$ Hz, corresponding to a motional heating rate of 18 quantum/second, and a phonon lifetime of $\tau_{coh} = 55.7$ ms.

The phase coherence and transfer efficiency

The performance of storage lifetime has been estimated by observing the evolution of the coherent and thermal occupancies back into a thermal state in equilibrium with its environment. We then study the coherence of using a silicon nitride mechanical oscillator as a memory. We choose four signal pulses of which the amplitudes (in a unit of quanta) and phases are chosen from the set of $\{(9, \pi/4), (6, 3\pi/4), (6, -3\pi/4), (7, -\pi/4)\}$. The phases of these four signal pulses are rotated in $\pi/2$ increments. Retroactive to the previous protocol depicted in Fig. 2a, we repeated the transfer-pulse sequences 8080 times (2040 repetitions per phase) and then obtained the state tomography of each retrieved microwave pulse in the quadrature phase-space. Figure 6a shows the measurement results, indicating that the phase of the signal pulse is faithfully recovered after storage. The distance from the center of each set

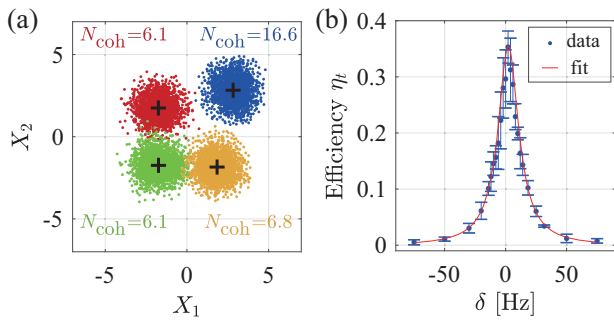


Fig. 6 The phase coherence and total transfer efficiency. **a** State tomography of four transmitted microwave pulses using the same measurement protocol described in Fig. 4a. The phases of four prepared signal pulses are rotated in increments of $\pi/2$, starting at $\pi/2$. The storage interval is $\tau = 1$ ms. Each color corresponds to an input pulse signal with a specific amplitude and phase. **b** The overall transfer efficiency for the memory. Blue-dot and red-solid curves represent the data and Lorentz fitting, respectively. Error bars represent the standard deviation of a data set. The black '+' marks the center of each group of scatterplots.

of scattering points to the coordinate origin (R) corresponds to the square root of the coherent component of the recovered microwave pulse, i.e., $R^2 = N_{\text{coh}}$. The data in Fig. 6a show that the device can store microwave coherent states into mechanical excitations with different amplitudes and phases, indicating the coherence of the memory device.

We then study another important figure of merit for characterizing a coherent memory, the overall transfer efficiency (η_t), which can be defined by the energy ratio of the retrieved (E_{out}) and input pulses (E_{in}), i.e., $\eta_t = (E_{\text{out}}/E_{\text{in}})$. The coherent portion of the retrieved signal is given by $E_{\text{out}} = \int_{t_3}^{+\infty} \langle V_{\text{out}}(t) \rangle^2 dt$. From time t_1 to t_2 in a transfer-pulse sequence [as depicted in Fig. 2a], the writing field (yields a transfer rate at γ_{opt} to all channels) can capture an itinerant microwave pulse, $V_{\text{in}} = V_{\text{pre}} \exp(\Gamma/2) \cos(\omega_s t)$, whose amplitude (energy) grows exponentially at rate $\Gamma/2$ (Γ), and the oscillation frequency is ω_s . The coherent energy of the bypass signal pulse can be expressed as $E_{\text{bp}} = \int_{-\infty}^{t_2} \langle V_{\text{out}}(t) \rangle^2 dt$. In the case of large frequency detuning between the signal pulse and the cavity resonator ($\delta = \omega_s - \omega_c \gg \kappa$), the total transfer efficiency equals zero and all energy of the input signal pulse is bypassed. At this point, the coherent portion (E_{bp}^{δ}) of the bypass signal exactly corresponds to the total energy of the input signal pulse. By setting the detuning to one megahertz ($\delta_L = 1$ MHz), we obtained the signal pulse energy (before being captured) based on the relation $E_{\text{in}} = E_{\text{bp}}^{\delta_L}$, which is used as the reference energy for the calculation of normalized total transfer efficiency.

Figure 6b shows the measured overall transfer efficiency η_t as a function of frequency detuning δ . The curve is in Lorentzian shape and the fitted bandwidth is given by $\Gamma_B = 19.54$ Hz, which keeps in corresponds with γ_{opt} introduced by the write field to the mechanical oscillator. When the write pulse frequency (ω_s) resonates with the eigenfrequency of the microwave cavity (ω_c), viz, $\delta = 0$, the transfer efficiency reaches the maximum value, $\eta_t = 0.356$. The Langevin equations for an optomechanical system imply that the maximum transfer efficiency is $\eta_m = (\kappa_e/\kappa)^2 = 0.363$. The total transfer efficiency depends on the energy conversion efficiency of the two steps, the state capture and retrieval, respectively. These two transfer steps are reciprocal with the same maximum transfer efficiency of $\eta = \kappa_e/\kappa$.

In our experiments, the measured maximum transmission efficiency approaches its theoretical limit by matching the signal pulse amplitude growth rate to the optical damping rate introduced by the sideband transmission field (see Supplementary Note 5), $\Gamma = \gamma_{\text{opt}}$. As initially pointed out and experimentally

verified in references^{58,59}, when $\Gamma \simeq \gamma_{\text{opt}}$, the writing field is well matched to the signal pulse (preparation field), and nearly complete absorption can be achieved. In contrast, when $\Gamma \gg \gamma_{\text{opt}}$ or $\Gamma \ll \gamma_{\text{opt}}$, all input signal pulses are bypassed because the writing field is poorly matched to the preparation pulse. Matching the transfer rate to the signal growth rate is a universal rule for achieving maximum overall efficiency for optomechanical memory.

The quantum threshold and memory fidelity

In the above sections we have demonstrated that the high-Q silicon nitride mechanical oscillator cooled down to ground-state provides a promising platform for realizing long-lived and coherent memory for microwave photons with different amplitudes and phases. We then study the state restoration fidelity F and compare it with the quantum threshold (also called as classical boundary), which is the minimum fidelity F_{min} required for a quantum memory. We consider the Uhlmann-Jozsa definition

of state transfer fidelity^{86,87}, $F = (\text{Tr}[(\sqrt{\rho_i} \rho_f \sqrt{\rho_i})^{1/2}])^2$, where ρ_i (ρ_f) is the density matrix of the initial stored state (final retrieved state), respectively. Since the state to be stored and transferred is a pure state, the general definition of the transfer fidelity reduces to^{88–90}, $F = \text{Tr}(\rho_i \rho_f)$. Hammerer et al. computed the quantum threshold for storage and transmission of coherent states⁹¹. The minimum fidelity F_{min} required for a quantum memory is given by $F_{\text{min}} = (1 + N_{\text{coh}})/(2N_{\text{coh}} + 1)$. Here, $N_{\text{coh}} = |a_n|^2$ is the average energy of the stored microwave pulse.

Figure 7 shows the state tomography and count distribution of the recovered microwave pulse from the mechanical memory. In quadrature phase space, the red-colored scatter dots and green scatter dots represent the captured, stored, and retrieved microwave fields with equal coherent energy N_{coh} , but with a phase difference of π . The black-colored scatter dots correspond to the state tomography of the mechanical ground state without coherent state storage, i.e., $N_{\text{coh}} = 0$. Figure 7 implies two features of the state transmission. The first is that the phase information of the signal pulses is faithfully recovered (with a π phase difference), which further verifies that the SiN-membrane-based optomechanical memory has phase coherence. The second feature is that as the coherent energy decreases, the center of the scatter dots will be submerged in the residual noise of the oscillator's ground state. As shown in Fig. 7(a), with coherent energy of $N_{\text{coh}} = 16$, the recovered microwave field, corresponding to the measured green (or red) scatter points, has no overlap with those scatter points of the mechanical oscillator in its ground state. When the coherent energy is decreased to e.g., $N_{\text{coh}} = 8.5$, Fig. 7b shows a partial overlap between the recovered state and mechanical background noise. In particular for $N_{\text{coh}} = 1.57$, Fig. 7c shows that the center of the scatterplot of the recovered microwave field enters the scattered area of the mechanical oscillator. For $N_{\text{coh}} = 0.4$, as shown in Fig. 7(d), the recovered microwave field and mechanical memory noise are not distinguishable. The corresponding Gaussian count distribution shown in Fig. 7 also exhibits similar state overlap behavior. As the coherent energy decreases, the center of the Gaussian distribution (marked by a white dashed line) of the recovered state gradually merges in the mechanical thermal state distribution regime.

It is worth noting that the amplitude and phase information can be faithfully recovered even for a stored coherent state with average energy below single photon/phonon, e.g., as shown in Fig. 7(d) for $N_{\text{coh}} = 0.4$. This is based on the state statistical distribution of multiple measurements. However, for a single measurement, how much amplitude and phase information can be recovered after the microwave state is stored and transmitted in a channel with thermal noise is related to the calculation of fidelity.

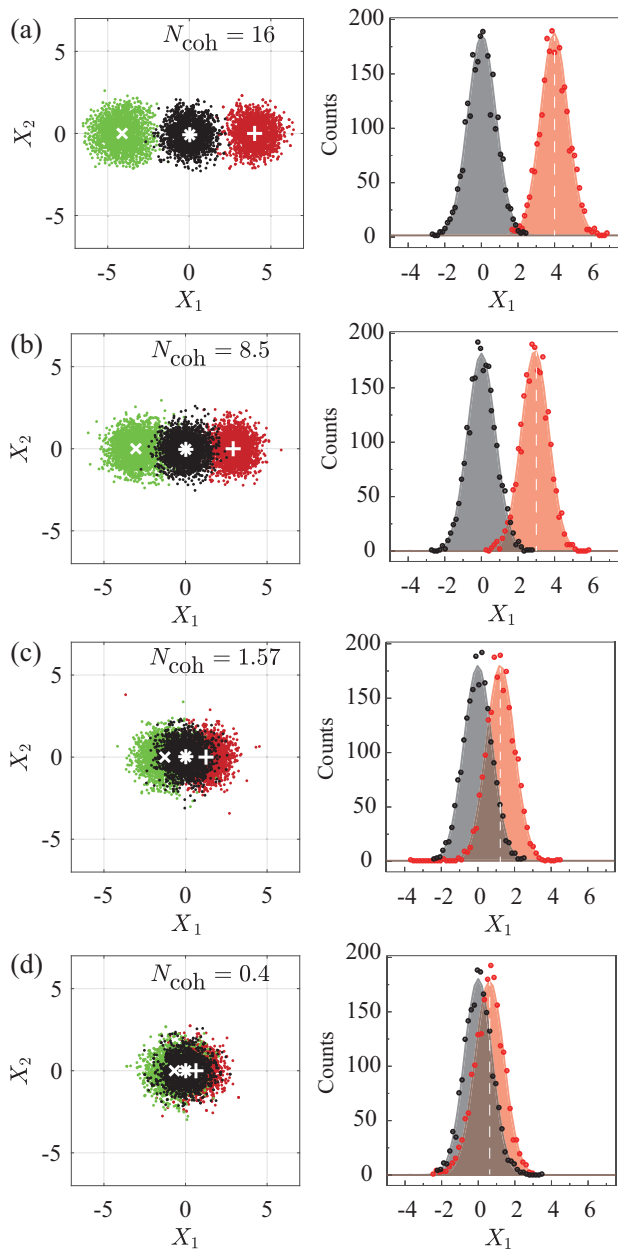


Fig. 7 Distribution overlaps in phase space. State tomography of two signal microwave pulses (the prepared fields) with same amplitudes but π phase difference. The red (green) colored scatter points represent the itinerant microwave field whose phase is fixed at zero (π). From (a–d) the coherent energies are $N_{\text{coh}} = [16, 8.5, 1.57, 0.4]$, respectively. The second column shows the corresponding Gaussian distributions of the recovered ground state and microwave field with zero-phase. The white-colored 'x', '*', '+' marks the center of each group of scatterplots.

The recovered microwave field is in a mixed state due to the thermal excitations of the mechanical memory. We then determine the density matrix ρ_f using a method of maximum likelihood state tomography⁵⁹. The density matrix is reconstructed through the RpR algorithm which maximizes the Likelihood function. The density matrix elements are updated after each iteration: $\rho^{t+1} = LR(\rho^t)\rho^t R(\rho^t)$, where L is the normalization parameter to satisfy that $\text{Tr}(\rho) = 1$.

The fidelity F as a function of stored coherent energy N_{coh} is shown in Fig. 8, with $N_{\text{sample}} = 2400$. The black-solid curve

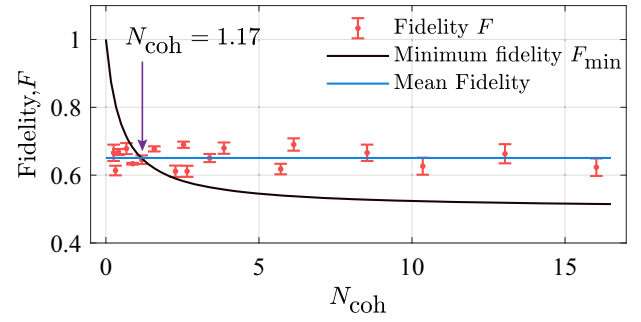


Fig. 8 Quantum threshold for coherent-state storage and measured fidelity in experiment. Measured fidelity (red dots with error bars) for the captured microwave field as a function of N_{coh} . The error bars are the standard deviation. Blue-solid line marks the mean fidelity and the black-solid curve is the quantum benchmark (threshold) for the storage and transmission of coherent states.

represents the quantum threshold, which corresponds to the minimum fidelity required for quantum memory. This criterion provides a benchmark for the coherent state storage and retrieval in the transmission channel with thermal and measurement noise⁹¹. The measured mean fidelity for our device is $F = 0.65$, corresponding to the coherent storage of a captured coherent state with a minimum average photon number of $N_{\text{coh}}^{\text{min}} = 1.17$. In order to realize quantum state storage of a captured coherent state at the single photon level, the fidelity should be improved over $F_s = 0.66$, which can be realized by further reducing the final thermal phonon occupation number of the mechanical memory oscillator. It is notable that the calculated fidelity here is about the storage and retrieval process. Taking the capture efficiency into consideration, the energy boundary (minimum average photon number) for quantum storage of a coherent state arriving at the input port is $N_{\text{in}}^{\text{min}} = 3.25$. The energy transfer efficiency η_t is not a critical limit, and it can be improved to near unity by designing the coupling of the waveguide and microwave cavity to be deeply over-coupled.

DISCUSSION

We have demonstrated microwave coherent state storage and retrieval in a absorptive-type cavity electromechanical memory device, which is constructed by flipping a metalized SiN membrane chip over an on-chip niobium microwave resonator. Turning on the transfer pulse sequence, the fundamental mechanical mode (memory mode) of the SiN membrane enters its ground state and can then be used to store the microwave photons as coherent mechanical excitations. The state capture efficiency has been optimized by matching the prepared field's exponential rising rate and the optical damping rate. Based on state tomography, we verify that the mechanical excitations as well as the stored coherent field undergo an energy decay at a rate of $\gamma_m/2\pi = 10$ mHz (corresponding to an energy decay time of $T_1 = 15.9$ s). The thermal decoherence rate arrives at $\Gamma_{\text{th}}/2\pi = 2.85$ Hz, indicating a long lifetime of $\tau_{\text{coh}} = 55.7$ ms, i.e., an 18 quantum/second motional heating rate. We have verified in experiment that both the amplitude and phase information of a microwave coherent state can be stored and retrieved, indicating the coherent property of this memory device. The overall energy transfer efficiency of the memory device is $\eta = 0.36$, and the measured fidelity for state storage and retrieval arrives at $F = 0.65$. That is to say, the device allows the retrieval of a stored coherent state with a minimum phonon number of $N_{\text{coh}}^{\text{min}} = 1.17$, corresponding to the coherent storage of an input coherent state with an energy of 3.25 photons. The overall energy transfer efficiency can be further improved to approach unity by designing the

external coupling of the waveguide and circuit resonator to be deeply over-coupled.

Toward operating this memory device at the single-photon level (i.e., realizing a quantum memory), the thermal occupation of mechanical resonator needs to be further reduced until the fidelity increases beyond the classical boundary (i.e., quantum threshold). At current stage, our experiment shows that SiN-membrane-based cavity electromechanical system is *long-lived* and *coherent* memory for the storage of microwave photons. The system studied in this work is a promising candidate for building microwave quantum memories. As a prospect, they can further implement hardware-efficient quantum error correction⁹² and will be an integrated part of the von-Neumann architecture for quantum computing systems based on superconducting circuits⁹³. Combined with band gap engineering⁹⁴, the quality factor of SiN membrane oscillators can be further improved, and the coherent storage time can be increased to the order of seconds. In the future, we can capture nonclassical states, including squeezed^{95–97} or entangled states^{98–100}, and store them inside long-lived mechanical memories. Obtaining long-lived macroscopic quantum states paves the way for fundamental tests of quantum mechanics in macroscopic objects^{78,101–103}.

METHODS

Device fabrication

The stoichiometric silicon nitride membrane is manufactured by Norcada with series number QX5050AS. Membrane windows ($500\ \mu\text{m} \times 500\ \mu\text{m} \times 50\ \text{nm}$) with 1.0 GPa high tensile stress are fabricated on a $500\ \mu\text{m}$ thick silicon frame. We use a commercial ACC μ RA flip-chip bonder to align the center of the square SiN membrane window with the center of the bottom coupling electrode of the microwave cavity. The planar resonant cavity was composed of an LC lumped element circuit, which was fabricated via a niobium (Nb) film (120 nm in thickness) on a high-resistance silicon (orientation of $\langle 100 \rangle$) substrate ($500\ \mu\text{m}$ in thickness). The Nb film is sputtered on the silicon (Si) substrate through physical vapor deposition (Syskey Technology, SP-IC4-A06). The sputtering pressure, sputtering power and sputtering time were 5×10^{-3} hPa, 150 W and 800 s, respectively. To mitigate the influence of oxidation on the resonator performance, the Nb film was placed in nitrogen (1000 Pa) for 30 min. The Nb/Si wafer was then subjected to the processes of coating, baking, exposure, development and reactive ion etching (RIE). The S1813 resist was selected as the coating layer, the spinning rate was 3000 rpm, and the operating time was 1 minute. The film with resist was then baked at $115\ ^\circ\text{C}$ for 2 min. The exposure process related to the pattern transfer was realized via the DWL 66+ laser lithography tool (Heidelberg Instruments). In the process of laser direct writing, the laser power, intensity, filter and focus were set at 100 mW, 55%, 5% and -20% , respectively. The development process was carried out at 1 minute in the MF-319 developer at room temperature. This was followed by rinsing in DIW fixing solution. After complete transfer, the LC resonator and associated circuits were obtained by the RIE process (RIE-10NR, Samco Inc).

State tomography in quadrature phase-space

The device is mounted on the 10 mK mixing-chamber plate of a commercial dilution refrigerator (Bluefors LD400). The cancelling line is combined with the output line by a directional coupler. By adjusting the amplitude and phase of the cancelling tone, the reflected pump tone (as well as the amplify tone) can be cancelled effectively to avoid saturation of the high electron mobility transistor (HEMT). The pump-tone (with frequency $\omega_c - \Omega_m$), amplify-tone (with frequency $\omega_c + \Omega_m$) and signal-tone (with frequency ω_c) are shaped to pulse by an arbitrary waveform generator (Tektronix AWG5014C) with mixer. These three tones are combined at room temperature with a splitter and transmitted down to the device. To

increase the on-off ratio of the pulse, we used a high-speed microwave switcher following the mixer at each tone. The control signal of the switch and the pulse signal of the mixer are generated simultaneously by the AWG in the marker channel and analog channel, respectively. A probe tone generated from PNA (Agilent N5232A) is also combined into the input line for device S parameter measurement. A real-time signal analyzer (Tektronix RSA5126B) is used to acquire the output signal. All instruments are phase-locked by a 10 MHz rubidium frequency standard. For the signal pulse measurement, the RSA acquiring frequency center is slightly shifted from signal-tone (fixed at $\omega_c/2\pi - 400\ \text{Hz}$) to make the acquired IQ signal have a small oscillation frequency. The delay time from write-in to read-out is controlled by the AWG in the time domain. To synchronize the RSA signal acquisition with the signal pulse, the RSA is triggered by an AWG pulse.

DATA AVAILABILITY

The authors declare that the main data that support the findings of this study are available within the article and its Supplementary Information. Additional data are available from the corresponding authors upon reasonable request.

CODE AVAILABILITY

The code generated in this work is available from the authors upon reasonable request.

Received: 11 January 2023; Accepted: 1 August 2023;

Published online: 11 August 2023

REFERENCES

- Blais, A., Grimsmo, A. L., Girvin, S. M. & Wallraff, A. Circuit quantum electrodynamics. *Rev. Mod. Phys.* **93**, 025005 (2021).
- Bao, Z. et al. On-demand storage and retrieval of microwave photons using a superconducting multiresonator quantum memory. *Phys. Rev. Lett.* **127**, 010503 (2021).
- Ma, L. et al. High-performance cavity-enhanced quantum memory with warm atomic cell. *Nat. Commun.* **13**, 2368 (2022).
- Kimble, H. J. The quantum internet. *Nature* **453**, 1023–1030 (2008).
- Lvovsky, A. I., Sanders, B. C. & Tittel, W. Optical quantum memory. *Nat. Photon.* **3**, 706–714 (2009).
- Simon, C. Towards a global quantum network. *Nat. Photon.* **11**, 678–680 (2017).
- Yu, Y. et al. Entanglement of two quantum memories via fibres over dozens of kilometres. *Nature* **578**, 240–245 (2020).
- Hofmann, J. et al. Heralded entanglement between widely separated atoms. *Science* **337**, 72–75 (2012).
- Moehring, D. L. et al. Entanglement of single-atom quantum bits at a distance. *Nature* **449**, 68–71 (2007).
- Hensen, B. et al. Loophole-free bell inequality violation using electron spins separated by 1.3 kilometres. *Nature* **526**, 682–686 (2015).
- Delteil, A. et al. Generation of heralded entanglement between distant hole spins. *Nat. Phys.* **12**, 218–223 (2016).
- Zhou, Z.-Q., Lin, W.-B., Yang, M., Li, C.-F. & Guo, G.-C. Realization of reliable solid-state quantum memory for photonic polarization qubit. *Phys. Rev. Lett.* **108**, 190505 (2012).
- Gündoğan, M., Ledingham, P. M., Kutluer, K., Mazzera, M. & De Riedmatten, H. Solid state spin-wave quantum memory for time-bin qubits. *Phys. Rev. Lett.* **114**, 230501 (2015).
- Zhong, M. et al. Optically addressable nuclear spins in a solid with a six-hour coherence time. *Nature* **517**, 177–180 (2015).
- Tang, J.-S. et al. Storage of multiple single-photon pulses emitted from a quantum dot in a solid-state quantum memory. *Nat. Commun.* **6**, 8652 (2015).
- Zhou, Z.-Q. et al. Quantum storage of three-dimensional orbital-angular-momentum entanglement in a crystal. *Phys. Rev. Lett.* **115**, 070502 (2015).
- Yang, T.-S. et al. Multiplexed storage and real-time manipulation based on a multiple degree-of-freedom quantum memory. *Nat. Commun.* **9**, 3407 (2018).
- Liu, X. et al. Heralded entanglement distribution between two absorptive quantum memories. *Nature* **594**, 41–45 (2021).
- Zhu, T.-X. et al. On-demand integrated quantum memory for polarization qubits. *Phys. Rev. Lett.* **128**, 180501 (2022).

20. Ma, Y., Ma, Y.-Z., Zhou, Z.-Q., Li, C.-F. & Guo, G.-C. One-hour coherent optical storage in an atomic frequency comb memory. *Nat. Commun.* **12**, 2381 (2021).
21. Liu, D.-C. et al. On-demand storage of photonic qubits at telecom wavelengths. *Phys. Rev. Lett.* **129**, 210501 (2022).
22. McGee, S. A., Meiser, D., Regal, C. A., Lehnert, K. W. & Holland, M. J. Mechanical resonators for storage and transfer of electrical and optical quantum states. *Phys. Rev. A* **87**, 053818 (2013).
23. Neuman, T. et al. A phononic interface between a superconducting quantum processor and quantum networked spin memories. *npj Quantum Inf.* **7**, 121 (2021).
24. Shandilya, P. K., Lake, D. P., Mitchell, M. J., Sukachev, D. D. & Barclay, P. E. Optomechanical interface between telecom photons and spin quantum memory. *Nat. Phys.* **17**, 1420–1425 (2021).
25. Barzanjeh, S. et al. Optomechanics for quantum technologies. *Nat. Phys.* **18**, 15–24 (2022).
26. Chu, Y. & Gröblacher, S. A perspective on hybrid quantum opto-and electro-mechanical systems. *Appl. Phys. Lett.* **117**, 150503 (2020).
27. Clerk, A. A., Lehnert, K. W., Bertet, P., Petta, J. R. & Nakamura, Y. Hybrid quantum systems with circuit quantum electrodynamics. *Nat. Phys.* **16**, 257–267 (2020).
28. Kurizki, G. et al. Quantum technologies with hybrid systems. *Proc. Natl Acad. Sci. USA* **112**, 3866–3873 (2015).
29. Dong, C., Wang, Y. & Wang, H. Optomechanical interfaces for hybrid quantum networks. *Natl Sci. Rev.* **2**, 510–519 (2015).
30. Rogers, B., Lo Gullo, N., De Chiara, G., Palma, G. M. & Paternostro, M. Hybrid optomechanics for quantum technologies. *Quantum Meas. Quantum Metrol.* **2**, 11–43 (2014).
31. Lambert, N. J., Rueda, A., Sedlmeir, F. & Schwefel, H. G. L. Coherent conversion between microwave and optical photons—an overview of physical implementations. *Adv. Quantum Technol.* **3**, 1900077 (2020).
32. Lauk, N. et al. Perspectives on quantum transduction. *Quantum Sci. Technol.* **5**, 020501 (2020).
33. Han, X., Fu, W., Zou, C.-L., Jiang, L. & Tang, H. X. Microwave-optical quantum frequency conversion. *Optica* **8**, 1050–1064 (2021).
34. Fiore, V., Dong, C., Kuzyk, M. C. & Wang, H. Optomechanical light storage in a silica microresonator. *Phys. Rev. A* **87**, 023812 (2013).
35. Fiore, V. et al. Storing optical information as a mechanical excitation in a silica optomechanical resonator. *Phys. Rev. Lett.* **107**, 133601 (2011).
36. Dong, C., Fiore, V., Kuzyk, M. C. & Wang, H. Transient optomechanically induced transparency in a silica microsphere. *Phys. Rev. A* **87**, 055802 (2013).
37. Lake, D. P., Mitchell, M., Sukachev, D. D. & Barclay, P. E. Processing light with an optically tunable mechanical memory. *Nat. Commun.* **12**, 663 (2021).
38. Wallucks, A., Marinković, I., Hensen, B., Stockill, R. & Gröblacher, S. A quantum memory at telecom wavelengths. *Nat. Phys.* **16**, 772–777 (2020).
39. MacCabe, G. S. et al. Nano-acoustic resonator with ultralong phonon lifetime. *Science* **370**, 840–843 (2020).
40. Aspelmeyer, M., Kippenberg, T. J. & Marquardt, F. Cavity optomechanics. *Rev. Mod. Phys.* **86**, 1391–1452 (2014).
41. Han, X., Zou, C.-L. & Tang, H. X. Multimode strong coupling in superconducting cavity piezoelectromechanics. *Phys. Rev. Lett.* **117**, 123603 (2016).
42. Blésin, T., Tian, H., Bhave, S. A. & Kippenberg, T. J. Quantum coherent microwave-optical transduction using high-overtone bulk acoustic resonances. *Phys. Rev. A* **104**, 052601 (2021).
43. Tian, H. et al. Hybrid integrated photonics using bulk acoustic resonators. *Nat. Commun.* **11**, 3073 (2020).
44. Hease, W. et al. Bidirectional electro-optic wavelength conversion in the quantum ground state. *PRX Quantum* **1**, 020315 (2020).
45. McKenna, T. P. et al. Cryogenic microwave-to-optical conversion using a triply resonant lithium-niobate-on-sapphire transducer. *Optica* **7**, 1737–1745 (2020).
46. Rueda, A. et al. Efficient microwave to optical photon conversion: an electro-optical realization. *Optica* **3**, 597–604 (2016).
47. Holzgrafe, J. et al. Cavity electro-optics in thin-film lithium niobate for efficient microwave-to-optical transduction. *Optica* **7**, 1714–1720 (2020).
48. Bochmann, J., Vainsencher, A., Awschalom, D. D. & Cleland, A. N. Nanomechanical coupling between microwave and optical photons. *Nat. Phys.* **9**, 712–716 (2013).
49. Hönl, S. et al. Microwave-to-optical conversion with a gallium phosphide photonic crystal cavity. *Nat. Commun.* **13**, 2065 (2022).
50. Andrews, R. W. et al. Bidirectional and efficient conversion between microwave and optical light. *Nat. Phys.* **10**, 321–326 (2014).
51. Higginbotham, A. P. et al. Harnessing electro-optic correlations in an efficient mechanical converter. *Nat. Phys.* **14**, 1038–1042 (2018).
52. Ockeloen-Korppi, C. F. et al. Low-noise amplification and frequency conversion with a multiport microwave optomechanical device. *Phys. Rev. X* **6**, 041024 (2016).
53. Lecocq, F., Clark, J. B., Simmonds, R. W., Aumentado, J. & Teufel, J. D. Mechanically mediated microwave frequency conversion in the quantum regime. *Phys. Rev. Lett.* **116**, 043601 (2016).
54. Tian, L. Adiabatic state conversion and pulse transmission in optomechanical systems. *Phys. Rev. Lett.* **108**, 153604 (2012).
55. Wang, Y.-D. & Clerk, A. A. Using interference for high fidelity quantum state transfer in optomechanics. *Phys. Rev. Lett.* **108**, 153603 (2012).
56. Mirhosseini, M., Sipahigil, A., Kalaee, M. & Painter, O. Superconducting qubit to optical photon transduction. *Nature* **588**, 599–603 (2020).
57. Delaney, R. D. et al. Superconducting-qubit readout via low-backaction electro-optic transduction. *Nature* **606**, 489–493 (2022).
58. Palomaki, T. A., Harlow, J. W., Teufel, J. D., Simmonds, R. W. & Lehnert, K. W. Coherent state transfer between itinerant microwave fields and a mechanical oscillator. *Nature* **495**, 210–214 (2013).
59. Reed, A. P. et al. Faithful conversion of propagating quantum information to mechanical motion. *Nat. Phys.* **13**, 1163–1167 (2017).
60. Thompson, J. D. et al. Strong dispersive coupling of a high-finesse cavity to a micromechanical membrane. *Nature* **452**, 72–75 (2008).
61. Xu, H., Jiang, L., Clerk, A. A. & Harris, J. G. E. Nonreciprocal control and cooling of phonon modes in an optomechanical system. *Nature* **568**, 65–69 (2019).
62. Weaver, M. J. et al. Coherent optomechanical state transfer between disparate mechanical resonators. *Nat. Commun.* **8**, 824 (2017).
63. Fedoseev, V., Luna, F., Hedgepeth, I., Löffler, W. & Bouwmeester, D. Stimulated raman adiabatic passage in optomechanics. *Phys. Rev. Lett.* **126**, 113601 (2021).
64. Dumont, V., Lau, H.-K., Clerk, A. A. & Sankey, J. C. Asymmetry-based quantum backaction suppression in quadratic optomechanics. *Phys. Rev. Lett.* **129**, 063604 (2022).
65. Norte, R. A., Moura, J. P. & Gröblacher, S. Mechanical resonators for quantum optomechanics experiments at room temperature. *Phys. Rev. Lett.* **116**, 147202 (2016).
66. Piergentili, P., Li, W., Natali, R., Vitali, D. & Di Giuseppe, G. Absolute determination of the single-photon optomechanical coupling rate via a hopf bifurcation. *Phys. Rev. Appl.* **15**, 034012 (2021).
67. Rossi, M. et al. Normal-mode splitting in a weakly coupled optomechanical system. *Phys. Rev. Lett.* **120**, 073601 (2018).
68. Sheng, J., Wei, X., Yang, C. & Wu, H. Self-organized synchronization of phonon lasers. *Phys. Rev. Lett.* **124**, 053604 (2020).
69. Peterson, R. W. et al. Laser cooling of a micromechanical membrane to the quantum backaction limit. *Phys. Rev. Lett.* **116**, 063601 (2016).
70. Chowdhury, A. et al. Quantum signature of a squeezed mechanical oscillator. *Phys. Rev. Lett.* **124**, 023601 (2020).
71. Yuan, M., Cohen, M. A. & Steele, G. A. Silicon nitride membrane resonators at millikelvin temperatures with quality factors exceeding 10^8 . *Appl. Phys. Lett.* **107**, 263501 (2015).
72. Yuan, M., Singh, V., Blanter, Y. M. & Steele, G. A. Large cooperativity and microkelvin cooling with a three-dimensional optomechanical cavity. *Nat. Commun.* **6**, 8491 (2015).
73. Liu, Y. et al. Optomechanical anti-lasing with infinite group delay at a phase singularity. *Phys. Rev. Lett.* **127**, 273603 (2021).
74. Wu, S. et al. Hybridized frequency combs in multimode cavity electromechanical system. *Phys. Rev. Lett.* **128**, 153901 (2022).
75. Liu, Y., Zhou, J., De Lépinay, L. M. & Sillanpää, M. A. Quantum backaction evading measurements of a silicon nitride membrane resonator. *N. J. Phys.* **24**, 083043 (2022).
76. Noguchi, A. et al. Ground state cooling of a quantum electromechanical system with a silicon nitride membrane in a 3d loop-gap cavity. *N. J. Phys.* **18**, 103036 (2016).
77. Seis, Y. et al. Ground state cooling of an ultracoherent electromechanical system. *Nat. Commun.* **13**, 1507 (2022).
78. Liu, Y., Mummery, J., Zhou, J. & Sillanpää, M. A. Gravitational forces between nonclassical mechanical oscillators. *Phys. Rev. Appl.* **15**, 034004 (2021).
79. Zhou, X. et al. High- q silicon nitride drum resonators strongly coupled to gates. *Nano Lett.* **21**, 5738–5744 (2021).
80. Pearson, A. N. et al. Radio-frequency optomechanical characterization of a silicon nitride drum. *Sci. Rep.* **10**, 1654 (2020).
81. Pokharel, A., Xu, H., Venkatachalam, S., Collin, E. & Zhou, X. Coupling capacitively distinct mechanical resonators for room-temperature phonon-cavity electromechanics. *Nano Lett.* **22**, 7351–7357 (2022).
82. Bağcı, T. et al. Optical detection of radio waves through a nanomechanical transducer. *Nature* **507**, 81–85 (2014).
83. Brubaker, B. M. et al. Optomechanical ground-state cooling in a continuous and efficient electro-optic transducer. *Phys. Rev. X* **12**, 021062 (2022).
84. Delaney, R. D., Reed, A. P., Andrews, R. W. & Lehnert, K. W. Measurement of motion beyond the quantum limit by transient amplification. *Phys. Rev. Lett.* **123**, 183603 (2019).
85. Massel, F. et al. Microwave amplification with nanomechanical resonators. *Nature* **480**, 351–354 (2011).
86. Uhlmann, A. The “transition probability” in the state space of a \ast -algebra. *Rep. Math. Phys.* **9**, 273–279 (1976).

87. Jozsa, R. Fidelity for mixed quantum states. *J. Mod. Opt.* **41**, 2315–2323 (1994).
88. Liang, Y.-C. et al. Quantum fidelity measures for mixed states. *Rep. Prog. Phys.* **82**, 076001 (2019).
89. Wang, Y.-D. & Clerk, A. A. Using dark modes for high-fidelity optomechanical quantum state transfer. *N. J. Phys.* **14**, 105010 (2012).
90. Teh, R. Y., Kiesewetter, S., Reid, M. D. & Drummond, P. D. Simulation of an optomechanical quantum memory in the nonlinear regime. *Phys. Rev. A* **96**, 013854 (2017).
91. Hammerer, K., Wolf, M. M., Polzik, E. S. & Cirac, J. I. Quantum benchmark for storage and transmission of coherent states. *Phys. Rev. Lett.* **94**, 150503 (2005).
92. Rosenblum, S. et al. Fault-tolerant detection of a quantum error. *Science* **361**, 266–270 (2018).
93. Mariani, M. et al. Implementing the quantum von Neumann architecture with superconducting circuits. *Science* **334**, 61–65 (2011).
94. Tsaturyan, Y., Barg, A., Polzik, E. S. & Schliesser, A. Ultracoherent nanomechanical resonators via soft clamping and dissipation dilution. *Nat. Nanotechnol.* **12**, 776–783 (2017).
95. Wollman, E. E. et al. Quantum squeezing of motion in a mechanical resonator. *Science* **349**, 952–955 (2015).
96. Pirkkalainen, J.-M., Damskägg, E., Brandt, M., Massel, F. & Sillanpää, M. A. Squeezing of quantum noise of motion in a micromechanical resonator. *Phys. Rev. Lett.* **115**, 243601 (2015).
97. Youssefi, A., Kono, S., Chegnizadeh, M. & Kippenberg, T. J. A squeezed mechanical oscillator with milli-second quantum decoherence. Preprint at <https://arxiv.org/abs/2208.13082> (2022).
98. Kotler, S. et al. Direct observation of deterministic macroscopic entanglement. *Science* **372**, 622–625 (2021).
99. Mercier de Lépinay, L., Ockeloen-Korppi, C. F., Woolley, M. J. & Sillanpää, M. A. Quantum mechanics-free subsystem with mechanical oscillators. *Science* **372**, 625–629 (2021).
100. Riedinger, R. et al. Remote quantum entanglement between two micro-mechanical oscillators. *Nature* **556**, 473–477 (2018).
101. Belenchia, A. et al. Testing quantum gravity induced nonlocality via optomechanical quantum oscillators. *Phys. Rev. Lett.* **116**, 161303 (2016).
102. Al Balushi, A., Cong, W. & Mann, R. B. Optomechanical quantum cavendish experiment. *Phys. Rev. A* **98**, 043811 (2018).
103. Westphal, T., Hepach, H., Pfaff, J. & Aspelmeyer, M. Measurement of gravitational coupling between millimetre-sized masses. *Nature* **591**, 225–228 (2021).

ACKNOWLEDGEMENTS

We thank for the fruitful discussions with Prof. Mika A. Sillanpää. This work is supported by the National Key Research and Development Program of China (Grant

No. 2022YFA1405200) and the National Natural Science Foundation of China (Grants No. 12004044, and No. 62074091). Y.L. acknowledges the support of Beijing Municipal Science and Technology Commission (Grant No. Z221100002722011).

AUTHOR CONTRIBUTIONS

Y.L. carried out the device design, fabrication and drafted the manuscript. Q.L. and Y.L. carried out the measurements. Y.L. conceived the project and coordinated the research. H.S. and T.L. helped draft and edit the manuscript. All authors analysed the measurement results and gave their final approval for publication. Y.L. and Q.L. contributed equally to this work.

COMPETING INTERESTS

The authors declare no competing interests.

ADDITIONAL INFORMATION

Supplementary information The online version contains supplementary material available at <https://doi.org/10.1038/s41534-023-00749-x>.

Correspondence and requests for materials should be addressed to Yulong Liu or Tiefu Li.

Reprints and permission information is available at <http://www.nature.com/reprints>

Publisher's note Springer Nature remains neutral with regard to jurisdictional claims in published maps and institutional affiliations.



Open Access This article is licensed under a Creative Commons Attribution 4.0 International License, which permits use, sharing, adaptation, distribution and reproduction in any medium or format, as long as you give appropriate credit to the original author(s) and the source, provide a link to the Creative Commons license, and indicate if changes were made. The images or other third party material in this article are included in the article's Creative Commons license, unless indicated otherwise in a credit line to the material. If material is not included in the article's Creative Commons license and your intended use is not permitted by statutory regulation or exceeds the permitted use, you will need to obtain permission directly from the copyright holder. To view a copy of this license, visit <http://creativecommons.org/licenses/by/4.0/>.

© The Author(s) 2023